

Article

A Nonlinear Gradient-Coiling Metamaterial for Enhanced Acoustic Signal Sensing

Guodong Hao , Xinsa Zhao and Jianning Han *

School of Information and Communication Engineering, North University of China, Taiyuan 030051, China; adeneogdhao@163.com (G.H.); xinsazhao@163.com (X.Z.)

* Correspondence: hanjn46@nuc.edu.cn

Abstract: Acoustic sensing systems play a critical role in identifying and determining weak sound sources in various fields. In many fault warning and environmental monitoring processes, sound-based sensing techniques are highly valued for their information-rich and non-contact advantages. However, noise signals from the environment reduce the signal-to-noise ratio (SNR) of conventional acoustic sensing systems. Therefore, we proposed novel nonlinear gradient-coiling metamaterials (NGCMs) to sense weak effective signals from complex environments using the strong wave compression effect coupled with the equivalent medium mechanism. Theoretical derivations and finite element simulations of NGCMs were executed to verify the properties of the designed metamaterials. Compared with nonlinear gradient acoustic metamaterials (Nonlinear-GAMs) without coiling structures, NGCMs exhibit far superior performance in terms of acoustic enhancement, and the structures capture lower frequencies and possess a wider angle acoustic response. Additionally, experiments were constructed and conducted using set Gaussian pulse and harmonic acoustic signals as emission sources to simulate real application scenarios. It is unanimously shown that NGCMs have unique advantages and broad application prospects in the application of weak acoustic signal sensing, enhancement and localization.

Keywords: acoustic metamaterial; weak sound perception; sound rainbow capture; equivalent medium; strong wave compression



Citation: Hao, G.; Zhao, X.; Han, J. A Nonlinear Gradient-Coiling Metamaterial for Enhanced Acoustic Signal Sensing. *Crystals* **2023**, *13*, 1291. <https://doi.org/10.3390/cryst13081291>

Academic Editors: Jihong Ma and George Kenanakis

Received: 6 July 2023

Revised: 6 August 2023

Accepted: 17 August 2023

Published: 21 August 2023



Copyright: © 2023 by the authors. Licensee MDPI, Basel, Switzerland. This article is an open access article distributed under the terms and conditions of the Creative Commons Attribution (CC BY) license (<https://creativecommons.org/licenses/by/4.0/>).

1. Introduction

Acoustic sensing technology is a highly effective technique in the field of remote sensing, utilizing the physical properties of sound [1–11]. In the last decade, considerable progress has been made in improving the signal-to-noise ratio (SNR) in electroacoustic sensor device applications. Ashiqur Rahaman et al. optimized the sensor structure by fusing aluminum nitride (AlN) and circular interfinger electrode patterns to improve the SNR [12]. Among them, it is essential to utilize intelligent algorithms to improve the signal-to-noise ratio [13–16]. Most recently, Xiang et al. proposed a robust speech enhancement method based on U-Net and generative adversarial learning to achieve speech enhancement at extremely low SNR conditions using algorithmic post-processing [17]. However, in practical engineering applications, some useful information in acoustic signals is weak, such as harmonic signals caused by structural damage [18–21]. Conventional cost-effective electrical sensor devices may not be able to sense these weak useful feature signals, and samples doped with strong background noise are difficult to train reliable models using deep learning. Therefore, there is an urgent need to develop a sound transmission system that can effectively perceive weak acoustic signals.

In recent years, acoustic metamaterial have emerged as a new material with the properties of manipulating sound energy, breaking through the acoustic performance limitations of traditional acoustic structures and materials. Due to their wide range of physical properties and extraordinary performance, such as acoustic bandgap [22], acoustic focusing [23,24],

acoustic vortex [25], and acoustic rainbow trapping [26–28], acoustic metamaterials have become critical in acoustic signal perception. In contrast to periodic metamaterials, metamaterials or media with gradient refractive index characteristics show flexible control of acoustic waves. In 2014, Chen et al. first proposed gradient acoustic metamaterials (GAMs) to achieve selective capture of different frequency band acoustic signals at different position gaps and gain on the captured acoustic signal amplitude. This demonstrated the structure's ability to modulate the spatial distribution of acoustic energy [29]. In 2019, Huang et al. proposed an improved gradient acoustic metamaterials structure (AMMs) with gradient curves, thickness and gap width, which achieved significant acoustic gain of more than one order of magnitude and was experimentally verified underwater [30,31]. In 2020, an acoustic superlattice structure with flat equifrequency bands and a strongly frequency-dependent refractive index was proposed [32]. In 2023, Wang et al. realized a miniaturized metamaterial device for non-adiabatic fast-wave compression and amplification based on the prototype GAMs [33]. In addition, the size of the metamaterial structures can also be reduced through the use of coiled structures with high refractive index media. In coiled structures, acoustic waves are forced to propagate through the channel system, which significantly lengthens the overall propagation time and results in low sound velocities and high refractive indices [34], as well as exceptionally high effective mass density and bulk modulus. Various acoustic wave modulation devices have been constructed in recent years using different spatial combinations of coiled channels, respectively [35–38]. In summary, both gradient metamaterials (GAMs) and coiled metamaterials have shown excellent performance in controlling acoustic wave propagation and spatial distribution of acoustic energy.

To realize broadband acoustically enhanced sensing, this article introduces nonlinear gradient-coiling metamaterials (NGCMs). Simulation results show that NGCMs possess higher acoustic enhancement capability, lower operating frequency, and a wider sensing range compared to nonlinear gradient metamaterials (Nonlinear-GAMs) without coiled structures, based on their acoustic rainbow capture capability. Experimental tests also demonstrate that NGCMs have superior acoustic response capability for both Gaussian pulse and harmonic acoustic signal detection.

The structure of this paper is organized as follows. In Section 2, the NGCM structure is designed and the properties of the model are analyzed theoretically. In Section 3, the acoustically enhanced nature of the structure is verified by performing finite element simulation analysis of the model. The operating frequency and multi-angle acoustic response of the NGCM structure are also investigated. In Section 4, experiments are conducted using Gaussian pulse and harmonic acoustic signals as the emission sources. The performance of the NGCM structure is tested in both time and frequency domains. In Section 5, the research results of the entire study are summarized.

2. Materials and Methods

2.1. Structural Design

The gradient structure shape designed in this paper is a nonlinear curved profile [30]. Compared with the linear profile proposed by Chen [29], the nonlinear profile can overcome the wave vector and mode field mismatch between the metamaterial waveguide and the background medium (air). Additionally, it improves the coupling efficiency between air and metamaterial. The structure consists of an array of 24 rectangular plates, as shown in Figure 1a (the top view of the structure). The coordinate origin is set at the center of the first plate. The width of the plate is described by the function. The units of this structure are millimeters (mm) and the coefficients a and b are set to $a = 0.0006$ and $b = 9$. The plate thickness is $t = 3$ mm and the gap between the plates is set to $c = 12$ mm. The metamaterial sample is fabricated by 3D printing technology using photosensitive resin (bulk modulus 2.65 GPa, density 1130 kg/m³). The height H of the sample is set to 90 mm. In order to increase the minimum threshold of sound pressure perception for this system, a coiled structure is incorporated between the air gap of this structure in this

paper. The first rectangular dentate structure is 4.5 mm from the midline, resulting in the construction of a rectangular air cavity with a width of 9 mm and a length of 12 mm. The rectangular denticles vary linearly in steps of $\Delta = 3$ mm, with each rectangular denticle having a thickness of $h = 3$ mm and a transverse length of $d = 9$ mm. Figure 1b provides a magnified view of the coiled cell. All parameter settings are summarized in Table 1. The parameters selected here are all appropriate values within a certain range to facilitate processing and experimental measurements. It is important to note that the outermost cell layout of the rectangular dentate structure must be smaller than the outermost dimension of the gradient structure to ensure that the acoustic properties of the gradient structure are not destroyed by the coiled structure.

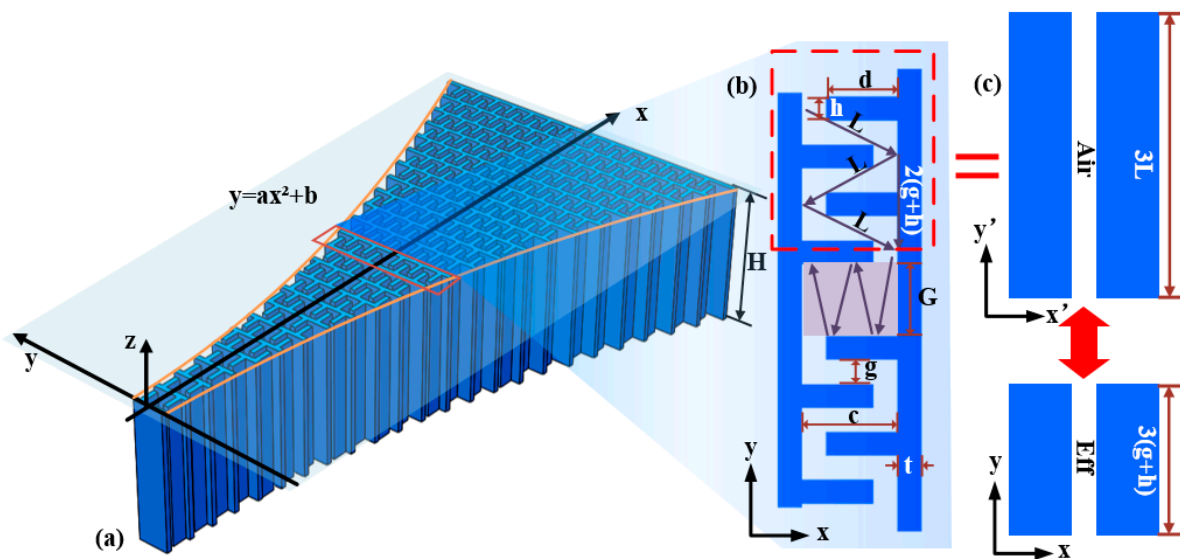


Figure 1. (a) Three-dimensional view of the structure of NGCMs; (b) enlarged two-dimensional view of the curled cells. (c) Schematic of the folded mapping in transformation acoustics.

Table 1. Values of characteristic parameters of NGCM structure.

Parameters	h	d	G	g	c	t	H
Values(mm)	3	9	9	3	12	3	90

2.2. Theoretical Analysis

Based on the characteristics of the NGCMs constructed above, a numerical model is developed to analyze their performance theoretically. The general homogeneous medium acoustic wave is controlled by its scalar fluctuation equation [39]:

$$\frac{\partial^2 P}{\partial t^2} = \frac{K}{\rho} \nabla^2 P \tag{1}$$

where P is the acoustic pressure. The acoustic velocity is given explicitly by $c = \sqrt{K/\rho}$. Huang et al. [40] used the equivalent medium theory to derive the mechanism of increasing acoustic pressure for nonlinear gradient structures. The effective mass density and bulk modulus can be expressed as

$$\rho = \frac{\rho_{res}\rho_{eff}}{(1 - F_r)\rho_{res} + F_r\rho_{eff}} \tag{2}$$

$$K = \frac{K_{res}K_{eff}}{(1 - F_r)K_{res} + F_rK_{eff}} \tag{3}$$

where F_r is the filling rate of the parallel plate. In Section 2, the constructed models of NGCMs are fabricated using photosensitive resins. The material has a density of $\rho_{res} = 1130 \text{ kg/m}^3$ and a bulk modulus of $K_{res} = 2.65 \text{ GPa}$. The air has a density of $\rho_{air} = 1.2 \text{ kg/m}^3$ and a bulk modulus of $K_{air} = 1.42 \times 10^5 \text{ Pa}$. Based on the transformation acoustics, the coiled structure between the two plates is calculated by the following equation [41]. In the long wavelength region, sound waves propagate below the cutoff frequency. Thus, the sawtooth path between the two plates is roughly equivalent to a long straight path. As shown in Figure 1, based on transform acoustics, the material parameter relationships between the long slot in air (with coordinates $x' - y'$, length L , bulk modulus K_{air} , and mass density ρ_{air}) and the short slot filled with metamaterials (with coordinates $x - y$, length l , bulk modulus K_{eff} , and mass density ρ_{eff}) can be written as $\rho_{eff}^{-1} = H\rho_{air}^{-1}H^T / \det(H)$ and $K_{eff} = \det(H) \times K_{air}$. H is the Jacobian matrix defined by $H = \text{diag}\{\partial x' / \partial x, \partial y' / \partial y\}$. Here, the fold mapping is specified by $y = y' / \beta$ and $x = x'$, where $\beta = L / (g + h)$ is the compression ratio of the coiled structure.

$$\rho_{eff}(x', y') = \begin{pmatrix} \beta & 0 \\ 0 & \frac{1}{\beta} \end{pmatrix} \rho_{air}(x, y) \tag{4}$$

$$K_{eff}(x', y') = \frac{K_{air}(x, y)}{\beta} \tag{5}$$

The computational derivation provides the mass density of $\rho_{eff} = \beta \cdot \rho_{air}$, bulk modulus of $K_{eff} = K_{air} / \beta$, and effective refractive index of $n_{eff} = \beta \cdot n_{air}$ for the coiled structure, The constructed model of NGCMs can be decomposed into an infinite number of approximations of uniform metamaterial cross sections, $y(x) = ax^2 + b$ is a function of the width of one side of NGCMs. The effective refractive indices of the metamaterials can be obtained as follows:

$$n_{NGCM}(x, f) = \sqrt{n_{eff} + \frac{K_{eff} \cdot \rho_{eff}}{\rho \cdot K} \left(\tan \left[2\pi f \cdot y(x) \cdot \sqrt{\frac{\rho}{K}} \right] \right)^2} \tag{6}$$

Here, f is the frequency of the incident acoustic wave and n_{air} is the refractive index of the air. The equation shows that N_{NGCM} is a function of frequency and the local width of the metamaterial plate. n_{eff} is a constant value controlled by the compression ratio of the coiled structure. Assuming that the thickness $y(x)$ of the metamaterial plate is a smooth function along the propagation direction, gradually increasing $y(x)$ can adjust the effective refractive index of the metamaterial system and result in a gradient distribution of the refractive index along the propagation direction.

For the analytical model, we use the Wentzel–Kramer–Brillouin (WKB) approximation to characterize the acoustic wave propagation along the conical metamaterial structure. Based on the solution of the effective refractive index of the above equation, the relationship between the sound pressure along the x -axis and the input frequency can be derived as

$$P_{NGCM}(x, f) = \frac{\sqrt{2\pi \cdot \rho_{eff} f} \cdot \sqrt[4]{1 - n_{NGLM}^{-2}}}{\cos \left[\arctan \left(\rho \cdot \rho_{eff}^{-1} \sqrt{n_{NGCM}^2 - 1} \right) \right]} \tag{7}$$

In comparison to the Nonlinear-GAM structure, the NGCM structure contains a coiled structure at the gap between the two plates, which increases the equivalent mass density and effective refractive index between the two plates while decreasing the bulk modulus. Substituting into Equations (6) and (7) results in an increase in n_{eff} and ρ_{eff} .

The above theory using equivalent media demonstrates that NGCMs can effectively amplify acoustic signals. Incident acoustic waves of different wavelengths are captured and enhanced at different locations [29]. From the microscopic point of view, the subwavelength coiled structure filled between the two partitions of the gradient structure results in various

gaps in the capture of acoustic signals with different frequencies. At the same time, as the propagation speed of sound waves in air is uniform, the sound waves will be propagated roughly along the path of Figure 1b (purple). The propagation distance of sound waves in the coiled structure is $2L = 2\sqrt{(g+h)^2 + c^2}$. The coiled structure causes the equivalent sound velocity between the slits to drop in comparison to the direct propagation distance $2(g+h)$, resulting in an increase in the structure's effective refractive index [41]. This increase in effective refractive index leads to an increase in sound wave amplitude. On one side of the sound waves through the coiled structure to the middle part of the structure gap, the amplitude value to further enhance, with the other side of the amplified sound waves to the cavity to form a resonance. Since the effective refractive index in the area of the coiled structure is greater than that of the intermediate cavity section, the sound waves reach the cavity section and encounter two reflectors on either side of the coiled structure. The sound waves resonate between these reflectors, further enhancing the sound signal amplitude, improving frequency selectivity, and causing the sound energy to dissipate slowly in the intermediate cavity. Moreover, the coiled structure between each gap increases the acoustic propagation distance. As a consequence, the operating frequency captured by the gap is reduced.

3. Simulation Analysis

To characterize the acoustic response of the metamaterial, the structure can be considered as a two-dimensional (2D) acoustic system in the simulation. In this paper, the 2D structure is constructed in the pressure acoustics module of Comsol Multiphysics v6.0, as shown in Figure 2. The gray area represents the air medium, and the structure can be considered as a rigid body. The boundary is set to be a hard sound field boundary (RB). A plane wave with an intensity of 1 Pa is used as the incident acoustic wave, which enters from the left side. To construct an ideal plane wave environment, a perfect matching layer (PML) is set on both sides and opposite sides of the incident plane wave port to absorb the reflected acoustic wave. To reduce the influence on the model sound field during the experiment, we place a Micro Electro Mechanical Systems Microphones (MEMS-MIC) at the central cavity edge position to detect the acoustic signal. Similarly, in the simulated environment, the probe point position is also set at the central cavity edge to observe the acoustic enhancement phenomenon between the air gaps, as shown in the orange point position in Figure 2. Here, the sound pressure gain value (PG) is used as an effective measure of the acoustic enhancement effect. It is defined as $PG = PM/PF$ [36,42,43], where PM denotes the sound pressure amplitude in NGCMs and PF denotes the sound pressure amplitude in the free space. The sound field transmission is then simulated to obtain the sound pressure gain value. Furthermore, this paper does not discuss the first six air gaps of the gradient structure due to the mismatch between the acoustic vector and the mode field [44]. In order to characterize the performance of NGCMs relative to Nonlinear-GAMs without added coiled structure, Nonlinear-GAM models are simultaneously constructed in this paper. After removing the coiled structure between the slits, the model parameters are consistent with those of the NGCMs ($c = 12$ mm, $t = 3$ mm, $H = 90$ mm). The center frequencies of each air gap (from the 7th to the last air gap) of the NGCM structure (f_{NGCM} in Hz) and Nonlinear-GAM structure (f_{GAM} in Hz) obtained from the simulation are listed in Tables 2 and 3.

The results in Table 2 show that, for the NGCM structure, the center frequencies of the 14th, 18th, 20th, and 22nd air gaps are 910 Hz, 650 Hz, 530 Hz, and 458 Hz, respectively. Figure 3a–d display the corresponding sound pressure distribution at these frequencies. For comparative analysis, Figure 3e–h show the sound pressure distribution at the center frequencies for the metamaterials with Nonlinear-GAM structure at the same gap positions. It can be observed that these frequencies are captured and enhanced at the 14th, 18th, 20th, and 22nd gap positions. The absolute sound pressure gain between different air gaps is obtained through simulation. Figure 4a,b display the absolute sound pressure gain curves for the NGCM structure and Nonlinear-GAM structure, respectively. For the 14th, 18th,

20th, and 22nd air gaps, the amplified sound pressure amplitudes are 54.2 times, 75.6 times, 103.4 times, and 57.6 times, respectively. Additionally, Figure 4a shows that the structure exhibits enhanced performance in a wider band range from 416 Hz to 944 Hz.

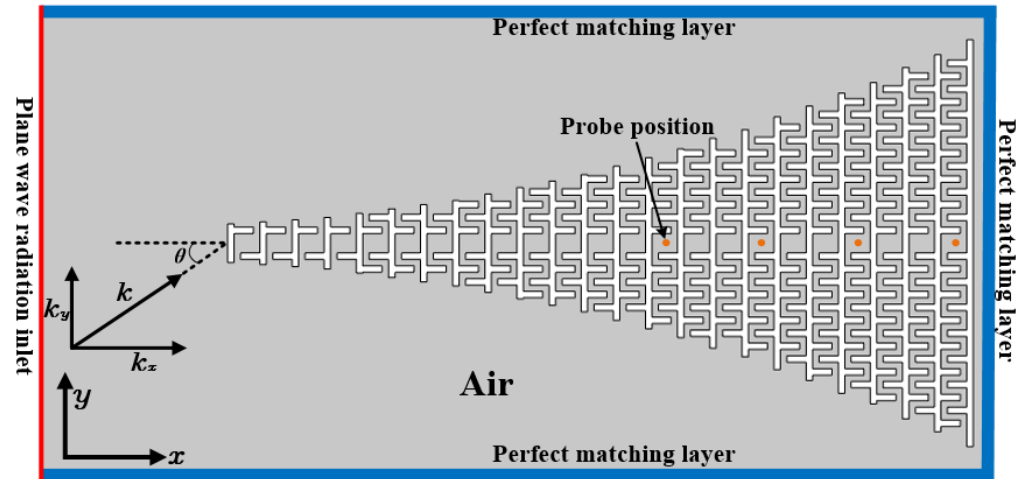


Figure 2. Two-dimensional structure of NGCMs and simulation boundary conditions.

Table 2. Center frequencies obtained for each air gap simulation for NGCM structure f_{NGCM} (Hz) and Nonlinear-GAM structure f_{GAM} (Hz).

Air Gaps	f_{NGCM} (Hz)	f_{GAM} (Hz)	Air Gaps	f_{NGCM} (Hz)	f_{GAM} (Hz)
7th	2292	3104	16th	810	1494
8th	1711	2774	17th	710	1365
9th	1702	2544	18th	650	1162
10th	1342	2411	19th	580	1168
11th	1340	2403	20th	530	1090
12th	1102	2196	21st	490	1010
13th	1100	1963	22nd	458	940
14th	910	1781	23rd	429	885
15th	821	1616			

Table 3. The center frequency calculated for each air gap value of NGCM structure F_{NGCM} (Hz) and Nonlinear-GAM structure F_{GAM} (Hz).

Air Gaps	F_{NGCM} (Hz)	F_{GAM} (Hz)	Air Gaps	F_{NGCM} (Hz)	F_{GAM} (Hz)
7th	2290	3103	16th	810	1494
8th	1712	2774	17th	710	1366
9th	1701	2544	18th	650	1161
10th	1342	2412	19th	580	1168
11th	1341	2402	20th	530	1090
12th	1102	2194	21st	490	1011
13th	1100	1963	22nd	458	940
14th	911	1782	23rd	429	884
15th	822	1616			

Based on the simulation analysis of the two structures with and without the coiled structure, the curves obtained at the same position of the gap frequency indicate that the average pressure amplitude can be amplified approximately 84.7 times in the NGCM structure, while the average pressure amplitude is amplified approximately 25 times in the Nonlinear-GAM structure. This phenomenon verifies the theoretical analysis presented in Section 2. Compared to the Nonlinear-GAM structure, the NGCM structure captures a lower frequency, which is approximately 43.2% lower. As mentioned, conventional gradient

materials require larger volume structures to capture lower frequency acoustic signals. The unique subwavelength coiled structure of the NGCM structure effectively solves this problem and provides a solution for the practical application of gradient structures. Additionally, the frequency domain profile of each slit in the NGCM structure is further enhanced compared to that of the Nonlinear-GAM structure, resulting in a narrower bandwidth of captured frequency domain between each slit.

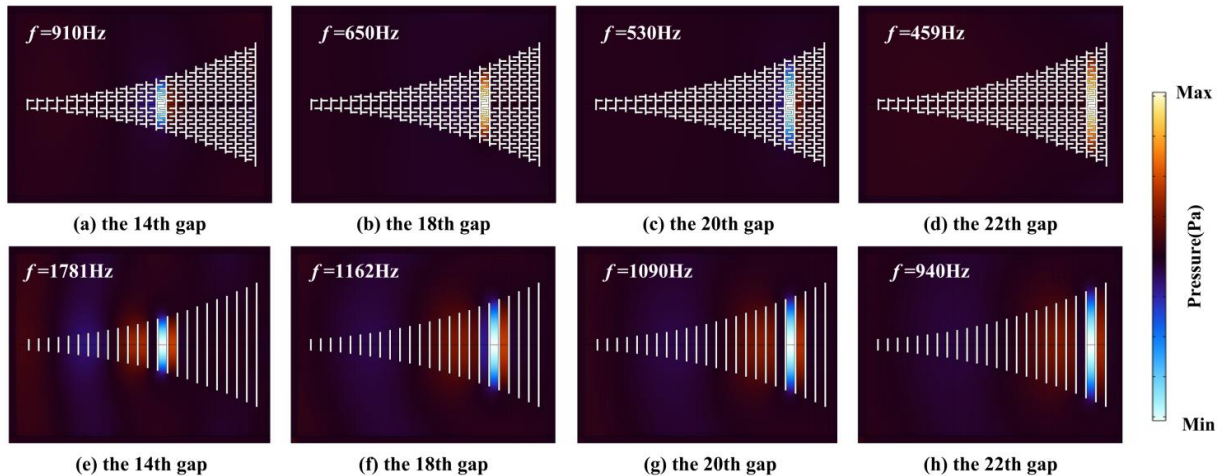


Figure 3. Simulation results of sound pressure distribution of two structures at different frequencies (a) NGCM structure $f = 910$ Hz; (b) NGCM structure $f = 650$ Hz; (c) NGCM structure $f = 530$ Hz; (d) NGCM structure $f = 459$ Hz; (e) Nonlinear-GAM structure $f = 1781$ Hz; (f) Nonlinear-GAM structure $f = 1162$ Hz; (g) Nonlinear-GAM structure $f = 1090$ Hz; (h) Nonlinear-GAM structure $f = 940$ Hz.

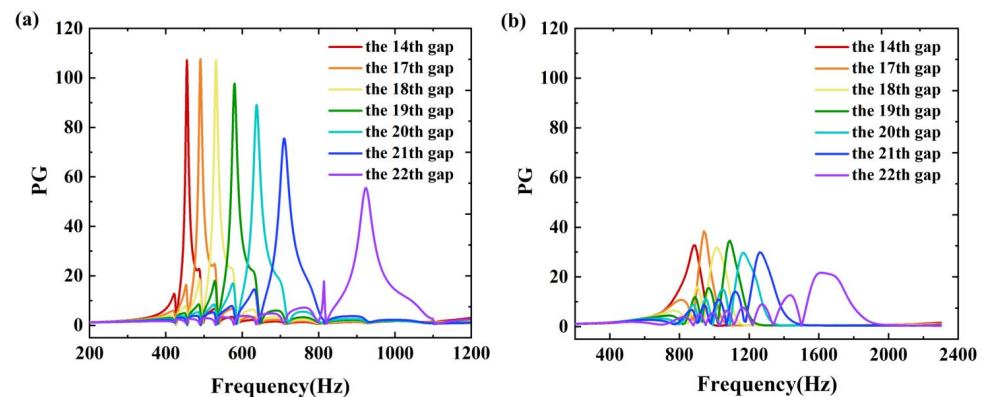


Figure 4. Absolute acoustic pressure gain between different air gaps (a) NGCM structure; (b) Nonlinear-GAM structure.

In addition, the acoustic responses of the gaps at different locations in the NGCMs and Nonlinear-GAMs are obtained using simulation calculations to show significant directionality. As shown in Figure 5, when the acoustic source is directly incident to the left side (π) of the NGCMs or Nonlinear-GAMs, the acoustic wave can be well coupled into the waveguide, which results in the highest acoustic pressure gain. With angular offset, the pressure gain of both structures gradually decreases. When the acoustic source is at an angle of 0.25π from the front of the metamaterial structure, the Nonlinear-GAMs no longer possess significant acoustic pressure gain, and the NGCMs still have gain response. At the angular positions ranging from 1.5π to 0.5π , the pressure gain is minimized due to the severe wave impedance mismatch at the interface between the NGCMs and the air. Therefore, this angular range is not used for research applications. Moreover, we construct practical experiments to validate the fitting of the above NGCM anisotropy. The experimen-

tal results show that the NGCMs has a wide sensing range of more than 180° compared to nonlinear-GAMs. The structure can be applied to more sound source localization scenarios by taking advantage of the structure's different response gain at different angles.

In addition, it was observed that the acoustic response of the gaps at different locations in the NGCM structure exhibited significant directionality. The polar plot of the maximum absolute total acoustic pressure gain of the metamaterial waveguide was obtained by finite element simulation and experimental correspondence, as shown in Figure 5. When the acoustic source is incident directly to the left (180°) of the NGCMs, the acoustic waves can be well coupled into the waveguide, resulting in the highest acoustic pressure gain. With the angular offset, the pressure gain gradually decreases. Nevertheless, the structure still has a gain response when the angle between the source and the NGCMs is 90° . At angular positions ranging from 105° to 255° , the pressure gain is minimized due to the severe wave impedance mismatch at the interface between the NGCMs and the air. Therefore, this angular range is not used in research applications. The structure can be applied to more sound source localization scenarios by taking advantage of the structure's different response gain at different angles. Moreover, the structure has a wide sensing range of more than 180° , which can help the sound source localization technology to obtain great progress.

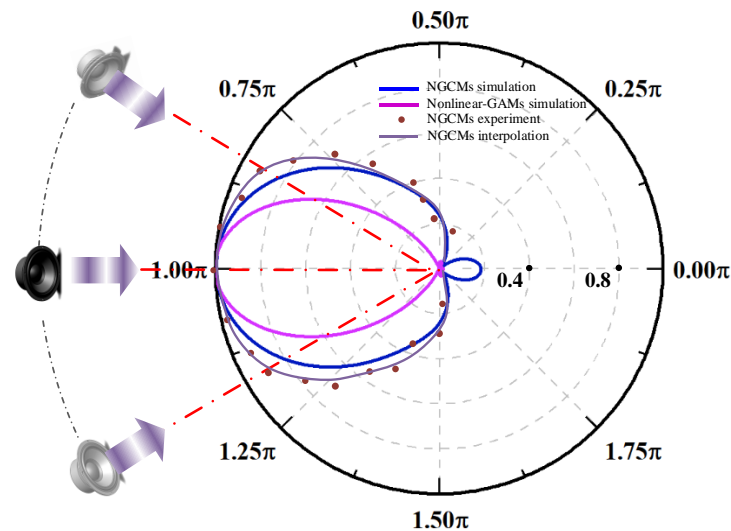


Figure 5. Schematic diagram of the directional response test: using Nonlinear-GAMs and NGCMs at a fixed position as a reference, simulations are used to obtain the normalized response of an ideal plane wave incident at different angles and the directional response of the NGCM structure for the actual experiment.

4. Experimental Validations

To evaluate the perceptual performance of the proposed NGCM structure in response to various specific signals, a test was carried out in this study. A host computer was applied to remotely control the audio signal output from the loudspeaker (width 100 mm, height 85 mm) via wireless transmission. Since the loudspeaker has a considerable size relative to metamaterial, we regard the sound wave emitted by the structure as an ideal plane wave. The acoustic device used is a MEMS-MIC (model: S15OT421-005) with a sensitivity of -42 dB and an amplification gain of 66. The bandwidth is from 100 Hz to 8 KHz and the signal-to-noise ratio is 59 dBA. The MEMS-MIC was positioned at the edge of the central cavity to capture the acoustic signal. In the absence of any acoustic signal, the output voltage of the MEMS-MIC remains floating at 1.5 V. The cross-sectional area of the MEMS-MIC probe used in the experiment is much smaller (3.06 mm^2) than the cross-sectional area of the interstitial cavity (108 mm^2). This enables the probe to be added to the test environment without significantly affecting the acoustic pressure distribution inside the metamaterial. The distance D between the speaker and the measurement position point is

0.45 m. Using the test gap as the reference point, the test environment (Figure 6) was built with the NGCM structure facing the speaker position at an angle of 0° .

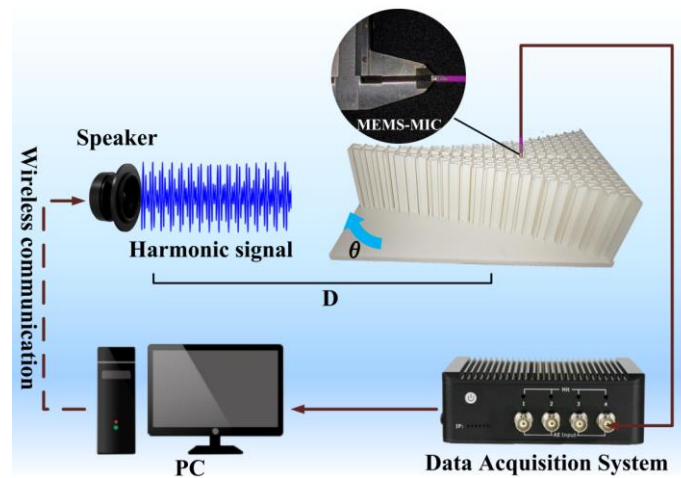


Figure 6. Signal detection test environment and experimental setup.

4.1. Pulse Signal Detection Based on NGCMs

Based on the characteristics of the impulse signal, the field of sound source localization techniques is mainly calculated by analyzing the received time domain acoustic signal [11,45,46]. Therefore, in this paper, the analysis of the impulse signal focuses on the time domain acoustic signal. The loudspeaker outputs a Gaussian pulse signal with a center frequency of 710 Hz. Figure 7a depicts the source of the pulse signal output from the loudspeaker, while Figure 7b shows the spectrum of the output signal. To facilitate comparative studies, the DC component of the voltage signal acquired by the MEMS-MIC is eliminated in this paper and only the AC component is preserved for analysis. This paper first compares the acoustic signals obtained from the 17th gaps and two adjacent gaps (Gap 16, Gap 18) for both the structure incorporating NGCMs and the structure without NGCMs, with the free sound field positions. Figure 7c shows the effective amplitude of the voltage signal from the MEMS-MIC output in a free sound field of 0.12 V. It can be seen that the Gaussian pulse signal is almost drowned out by the ambient noise after the target acoustic signal has been transmitted for some distance. The acquired signal-to-noise ratio is 3.1 dB. Figure 7d–f depict the acoustic signals received at gaps 16, 17, and 18, respectively, with effective voltage amplitudes of 0.36 V, 0.98 V, and 0.96 V. The obtained signal-to-noise ratios were 3.8 dB, 8.15 dB and 8.06 dB, respectively. It is evident that the sound pressure amplitude at gap 17 is considerably higher than that obtained at gap 16. Compared to the signal-to-noise ratio obtained without the addition of the metamaterial structure, the signal-to-noise ratio is significantly improved by approximately 5 dB. However, the sound pressure amplitude obtained at gap 18 is more comparable to that obtained at gap 17. We further measured the acoustic signals at the 19th and 20th gap positions. Figure 7g,h illustrate that the effective amplitudes obtained by the NGCMs at the 19th and 20th gaps are 0.37 V and 0.29 V, respectively. The corresponding signal-to-noise ratios are 3.92 dB and 2.86 dB, respectively. This study compared the effective amplitude of the sound pressure at the 17th gap position with and without the NGCM structure. It was discovered that the effective amplitude was amplified by a factor of 8.17, indicating the effectiveness of the NGCM structure in enhancing sound signals. Moreover, the moment of peak sound pressure with the NGCM structure was found to be delayed by 4 ms when compared to the moment of peak sound pressure in the free sound field, which was used as a reference. This is mainly due to the increased distance of the acoustic signal to the 17th gap measurement position, resulting from the coiled structure in the NGCMs, which exhibits a delayed effect of the peak acoustic signal at the measurement position. In future practical engineering

applications, the propagation time of the acoustic signal through the coiled structure of the measured position gap can be calculated to compensate for the time delay observed in the tested acoustic signals. This compensation can reduce the momentary error of the NGCM structure in perceiving impulse signals, thereby enhancing the accuracy of sound source localization. Furthermore, the experimental findings indicate that in practical applications, the center frequency of each gap may be slightly shifted due to sample processing errors, resulting in the center frequency of the target acoustic signal being between the center frequencies of gaps 17 and 18 of the NGCM structure. As a result, the effective amplitudes obtained at gaps 17 and 18 are relatively similar. By comparing the effective voltage amplitudes obtained at gaps 16, 19 and 20 with the target gap 17, it is evident that the signal amplitude at gap 17 is much greater than that obtained at gaps 16, 19 and 20. This suggests that the NGCMs exhibit distinct frequency selectivity for each gap when amplifying the acoustic signal.

4.2. Directional Acoustic Sensing of Harmonic Signals Based on NGCMs

In the context of environmental monitoring in specific regions, accurate extraction of feature signals is particularly important for exploration safety and feature classification [11,47–49]. For feature signal extraction, it is crucial to improve the signal-to-noise ratio of hidden feature signals in noisy environments by filtering out noise or enhancing the target signal. This article uses harmonic signals emitted by speakers to simulate characteristic signals in special environments. The harmonic signal is

$$P(t) = 15 \times \cos(2\pi \times f_1 \times t) + \cos(2\pi \times f_0 \times t) \quad (8)$$

where the target frequency $f_0 = 580$ Hz and the disturbance frequency $f_1 = 1080$ Hz. The frequency domain analysis of the original harmonic signal is illustrated in Figure 8a. The NGCM structure is positioned in the direction of the sound source based on the persistent harmonic signal by taking the 19th gap as the reference point and varying the theta angle. Starting from the vertical speaker position angle, the NGCMs are rotated clockwise and the sound pressure signal at gap 19 is captured using the MEMS-MIC. The main focus of this paper is on the study of the different angular amplitudes of the received acoustic signals. Therefore, the acquired acoustic signal is analyzed in the frequency domain and the spectrum obtained from the calculation is processed by normalization. The spectra of the harmonic signals at positions 75° , 45° , 15° and 0° were obtained (Figure 8(c1–c4)). Upon comparing the spectra of the acoustic signals obtained at various angles, it is observed that the NGCMs exhibit a significant gain in the signal amplitude of the target frequency component when the angle between the source position and the tip position of the NGCMs is 75° . In addition, the NGCMs demonstrate the capability to amplify the scrambled frequency component signal, with a maximum amplification effect of approximately 1.38 times that of the original scrambled frequency component. This phenomenon can be attributed to the incident acoustic waves encountering the coiled structures present on either side of the NGCMs. These structures localize the incident acoustic waves in the cavity at a wider operating frequency range, thereby allowing the same amplification effect to be achieved for the perturbed frequency components. Nonetheless, as the tip position of the NGCMs gradually approaches the source direction, the amplitude of the target frequency component (f_0) progressively increases. Eventually, it becomes 1.8 times the amplitude of the disturbance frequency component (f_1) and 26.7 times the amplitude of the original f_0 frequency component. In practical scenarios, the target frequency may be present as an ambiguous and unknown frequency component. The change in acoustic energy enhancement can be detected for each gap by turning the NGCMs at different angles. Figure 8(d1–d3,e1–e3) illustrates the spectra obtained at various angles for the 19th gap and its adjacent gaps (18th and 20th gaps). The characteristic signal frequency f_0 can be estimated by comparing the variations in the frequency components of gap 19 and its neighboring gaps at different angles. This approach leverages the frequency-selective enhancement feature of NGCMs, facilitating the identification of unknown target signals.

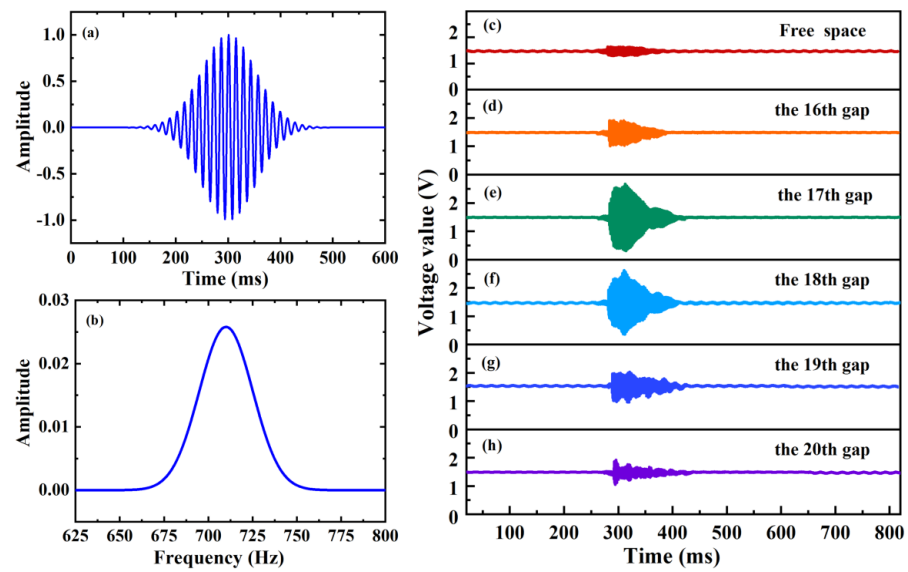


Figure 7. (a) Emitted pulse signal; (b) spectrogram of the emitted pulse signal; (c–h) voltage signal amplitude output from the MEMS-MIC at the tart gap position in the free acoustic field without the NGCM structure and at different positions of the gap with the NGCM structure.

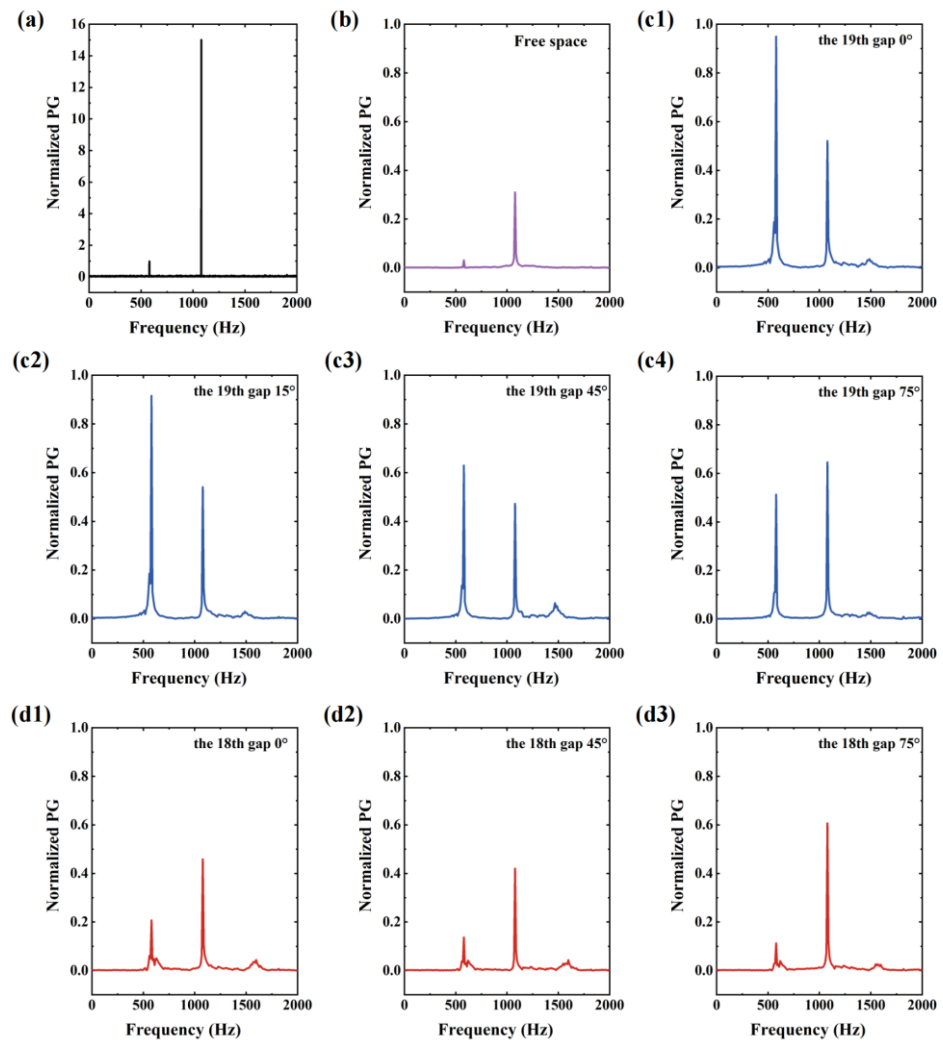


Figure 8. Cont.

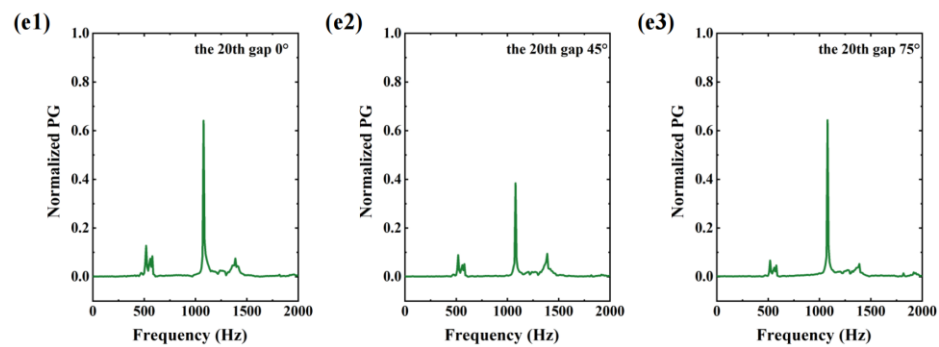


Figure 8. (a) Spectrum of the original harmonic signal; (b) spectrum of free space; (c1–c4) spectrum of the 19-gap harmonic signal at 0° , 15° , 45° , and 75° ; (d1–d3) spectrum of 18-gap harmonic signal at 0° , 45° , and 75° ; (e1–e3) spectrum of 20-gap harmonic signal at 0° , 45° , and 75° .

5. Conclusions

Traditional microphones have the limitations of difficult perception of weak acoustic signals and low SNR. To overcome this problem, we proposed a structure of NGCMs to achieve the effect of amplifying large values of weak acoustic signals at target frequencies, based on the strong wave compression effect coupled with the equivalent medium mechanism. It was also evaluated and verified through practical experiments for Gaussian acoustic signal time domain analysis and harmonic signal frequency domain analysis from different angles, respectively. The conclusions are summarized as follows:

- (1) The proposed NGCM structure can amplify the average pressure amplitude of the acoustic signal by a factor of approximately 84.7, which is superior to the Nonlinear-GAM model without the inclusion of the coiled structure.
- (2) Compared to conventional gradient models, NGCMs can operate at a reduced frequency without any change in volume.
- (3) The NGCM structure has a narrower bandwidth per slit, making the structure more frequency selective.
- (4) The structure has a wider angular range of acoustic response and is anisotropic, which helps NGCMs to work more efficiently in the context of localization of weak acoustic signals.
- (5) During the actual experimental measurements, it was found that the presence of the coiled structure in the structure delayed the arrival time at the measurement point. This paper proposes that the measurement time in the center of the gap of the NGCMs can be compensated by calculating the sound propagation time of the unilateral coiled structure with different gaps, thus reducing the error in the localization of the sound source.

It is foreseeable that, in the future, NGCMs will be used in practical engineering applications due to their unique advantages in the context of sensing target signals in the face of complex environmental noise.

Author Contributions: Conceptualization, G.H.; methodology, X.Z.; software, G.H.; validation, X.Z.; formal analysis, G.H.; investigation, G.H.; resources, J.H.; data curation, G.H.; writing—original draft preparation, G.H.; writing—review and editing, X.Z.; visualization, X.Z.; supervision, J.H.; funding acquisition, J.H. All authors have read and agreed to the published version of the manuscript.

Funding: The work was supported by Shanxi Scholarship Council of China, grant number 2023-127, the Natural Science Foundation of Shanxi Province, grant number 202103021224201, the National Natural Science Foundation of China, grant number 61671414, and the National Major Scientific Instrument Research Project of NSFC, grant number 61927807.

Data Availability Statement: Data will be available on reasonable request.

Conflicts of Interest: The authors declare no conflict of interest. The funders had role in the writing of the manuscript and in the decision to publish the results.

References

1. Shanyavskiy, A.A.; Banov, M.D. Durability diagnostics of turbine blades based on non-destructive acoustic emission testing. *Procedia Struct. Integr.* **2019**, *23*, 57–62. [[CrossRef](#)]
2. Khaled, A.Y.; Ekramirad, N.; Parrish, C.A.; Eberhart, P.S.; Doyle, L.E.; Donohue, K.D.; Villanueva, R.T.; Adedeji, A.A. Non-destructive detection of codling moth infestation in apples using acoustic impulse response signals. *Biosyst. Eng.* **2022**, *224*, 68–79. [[CrossRef](#)]
3. Donskoy, D.; Liu, D. Vibro-acoustic modulation baseline-free non-destructive testing. *J. Sound Vib.* **2021**, *492*, 115808. [[CrossRef](#)]
4. Augereau, F.; Roque, V.; Robert, L.; Despau, G. Non-destructive testing by acoustic signature of damage level in 304L steel samples submitted to rolling, tensile test and thermal annealing treatments. *Mater. Sci. Eng. A* **1999**, *266*, 285–294. [[CrossRef](#)]
5. Zhu, S.; Zhang, G.; Wu, D.; Jia, L.; Zhang, Y.; Geng, Y.; Liu, Y.; Ren, W.; Zhang, W. High Signal-to-Noise Ratio MEMS Noise Listener for Ship Noise Detection. *Remote Sens.* **2023**, *15*, 777. [[CrossRef](#)]
6. Borrelli, M.; Legare, B.; McCormack, B.; dos Santos, P.P.; Solazzo, D. Absolute Localization of Targets Using a Phase-Measuring Sidescan Sonar in Very Shallow Waters. *Remote Sens.* **2023**, *15*, 1626. [[CrossRef](#)]
7. De Marco, R.; Di Nardo, F.; Lucchetti, A.; Virgili, M.; Petetta, A.; Li Veli, D.; Screpanti, L.; Bartolucci, V.; Scaradozzi, D. The Development of a Low-Cost Hydrophone for Passive Acoustic Monitoring of Dolphin's Vocalizations. *Remote Sens.* **2023**, *15*, 1946. [[CrossRef](#)]
8. García, L.; Mota, S.; Titos, M.; Martínez, C.; Segura, J.C.; Benítez, C. Fiber Optic Acoustic Sensing to Understand and Affect the Rhythm of the Cities: Proof-of-Concept to Create Data-Driven Urban Mobility Models. *Remote Sens.* **2023**, *15*, 3282. [[CrossRef](#)]
9. Sun, Z.; Yang, S.; Zhang, F.; Lu, J.; Wang, R.; Ou, X.; Lei, A.; Han, F.; Cen, W.; Wei, D.; et al. A Reconstructed Method of Acoustic Logging Data and Its Application in Seismic Lithological Inversion for Uranium Reservoir. *Remote Sens.* **2023**, *15*, 1260. [[CrossRef](#)]
10. Wang, J.; Li, H.; Huo, G.; Li, C.; Wei, Y. Multi-Modal Multi-Stage Underwater Side-Scan Sonar Target Recognition Based on Synthetic Images. *Remote Sens.* **2023**, *15*, 1303. [[CrossRef](#)]
11. Wang, Z.; Ma, Y.; Kan, G.; Liu, B.; Zhou, X.; Zhang, X. An Inversion Method for Geoacoustic Parameters in Shallow Water Based on Bottom Reflection Signals. *Remote Sens.* **2023**, *15*, 3237. [[CrossRef](#)]
12. Rahaman, A.; Park, C.H.; Kim, B. Design and characterization of a MEMS piezoelectric acoustic sensor with the enhanced signal-to-noise ratio. *Sens. Actuators A Phys.* **2020**, *311*, 112087. [[CrossRef](#)]
13. Chu, H.; Li, C.; Wang, H.; Wang, J.; Tai, Y.; Zhang, Y.; Yang, F.; Benezeth, Y. A deep-learning based high-gain method for underwater acoustic signal detection in intensity fluctuation environments. *Appl. Acoust.* **2023**, *211*, 109513. [[CrossRef](#)]
14. Jung, Y.H.; Hong, S.K.; Wang, H.S.; Han, J.H.; Pham, T.X.; Park, H.; Kim, J.; Kang, S.; Yoo, C.D.; Lee, K.J. Flexible Piezoelectric Acoustic Sensors and Machine Learning for Speech Processing. *Adv. Mater.* **2020**, *32*, 1904020. [[CrossRef](#)] [[PubMed](#)]
15. Cha, Y.-J.; Mostafavi, A.; Benipal, S.S. DNoiseNet: Deep learning-based feedback active noise control in various noisy environments. *Eng. Appl. Artif. Intell.* **2023**, *121*, 105971. [[CrossRef](#)]
16. Kantamaneni, S.; Charles, A.; Babu, T.R. Speech enhancement with noise estimation and filtration using deep learning models. *Theor. Comput. Sci.* **2023**, *941*, 14–28. [[CrossRef](#)]
17. Hao, X.; Su, X.; Wang, Z.; Zhang, H.; Batushiren, A. UNetGAN: A Robust Speech Enhancement Approach in Time Domain for Extremely Low Signal-to-Noise Ratio Condition. In Proceedings of the Interspeech 2019, Graz, Austria, 15–19 September 2019; International Speech Communication Association: Baixas, France, 2019; pp. 1786–1790. [[CrossRef](#)]
18. Duane, D.; Zhu, C.; Piavsky, F.; Godø, O.R.; Makris, N.C. The Effect of Attenuation from Fish on Passive Detection of Sound Sources in Ocean Waveguide Environments. *Remote Sens.* **2021**, *13*, 4369. [[CrossRef](#)]
19. Khabotov, A.G.; Kalinina, V.I.; Khil'ko, A.I.; Malekhanov, A.I. Novel Neuron-like Procedure of Weak Signal Detection against the Non-Stationary Noise Background with Application to Underwater Sound. *Remote Sens.* **2022**, *14*, 4860. [[CrossRef](#)]
20. Bovsunovsky, A.; Nosal, O. Highly sensitive methods for vibration diagnostics of fatigue damage in structural elements of aircraft gas turbine engines. *Procedia Struct. Integr.* **2022**, *35*, 74–81. [[CrossRef](#)]
21. Yin, T.; Ng, C.-T.; Kotousov, A. Damage detection of ultra-high-performance fibre-reinforced concrete using a harmonic wave modulation technique. *Constr. Build. Mater.* **2021**, *313*, 125306. [[CrossRef](#)]
22. Zhang, S.; Zhang, Y.; Lu, W.; Hu, G.; Xu, B.; Cao, W. Low-frequency forbidden bandgap engineering via a cascade of multiple 1D superlattices. *J. Appl. Phys.* **2018**, *124*. [[CrossRef](#)]
23. Chen, D.-C.; Zhu, X.-F.; Wei, Q.; Yao, J.; Wu, D.-J. Broadband tunable focusing lenses by acoustic coding metasurfaces. *J. Phys. D Appl. Phys.* **2020**, *53*, 255501. [[CrossRef](#)]
24. Chen, D.-C.; Zhu, X.-F.; Wei, Q.; Wu, D.-J. Bidirectional asymmetric acoustic focusing with two flat acoustic metasurfaces. *Chin. Phys. B* **2018**, *27*, 124302. [[CrossRef](#)]
25. Li, X.-R.; Jia, Y.-R.; Luo, Y.-C.; Yao, J.; Wu, D.-J. Mixed focused-acoustic-vortices generated by an artificial structure plate engraved with discrete rectangular holes. *Appl. Phys. Lett.* **2021**, *118*, 043503. [[CrossRef](#)]
26. Xu, B.; Wu, J.; Lu, W.; Gu, X.; Zhang, L.; Zhang, S.; Zhang, Y. Transmission and rainbow trapping of acoustic waves in a fluid medium using gradient-index superlattices. *J. Appl. Phys.* **2021**, *129*, 154501. [[CrossRef](#)]
27. Zhu, J.; Chen, Y.; Zhu, X.; Garcia-Vidal, F.J.; Yin, X.; Zhang, W.; Zhang, X. Acoustic rainbow trapping. *Sci. Rep.* **2013**, *3*, 1728. [[CrossRef](#)]
28. Ni, X.; Wu, Y.; Chen, Z.-G.; Zheng, L.-Y.; Xu, Y.-L.; Nayar, P.; Liu, X.-P.; Lu, M.-H.; Chen, Y.-F. Acoustic rainbow trapping by coiling up space. *Sci. Rep.* **2014**, *4*, 7038. [[CrossRef](#)]

29. Chen, Y.; Liu, H.; Reilly, M.; Bae, H.; Yu, M. Enhanced acoustic sensing through wave compression and pressure amplification in anisotropic metamaterials. *Nat. Commun.* **2014**, *5*, 5247. [[CrossRef](#)]
30. Huang, X.; Yan, Y.; Ma, J.; Li, J.; Rui, X. An Acoustic Metamaterial-Based Sensor Capable of Multiband Filtering and Amplification. *IEEE Sens. J.* **2020**, *20*, 4413–4419. [[CrossRef](#)]
31. Li, J.; Shi, W.; Huang, X.; Ma, J.; Rui, X.; Guo, L. Study on a gradient structure acoustic metamaterial for underwater sound sensing enhancements. In Proceedings of the 2019 14th IEEE International Conference on Electronic Measurement & Instruments (ICEMI), Changsha, China, 1–3 November 2019; pp. 873–879.
32. Zubov, Y.; Djafari-Rouhani, B.; Jin, Y.; Sofield, M.; Walker, E.; Neogi, A.; Krokhin, A. Long-range nonspreading propagation of sound beam through periodic layered structure. *Commun Phys.* **2020**, *3*, 155. [[CrossRef](#)]
33. Wang, X.; Li, J.; Yang, J.; Chen, B.; Liu, S.; Chen, Y. Compact acoustic amplifiers based on non-adiabatic compression of sound in metamaterial waveguides. *Appl. Acoust.* **2023**, *204*, 109246. [[CrossRef](#)]
34. Li, Y.; Liang, B.; Tao, X.; Zhu, X.; Zou, X.; Cheng, J. Acoustic focusing by coiling up space. *Appl. Phys. Lett.* **2012**, *101*, 233508. [[CrossRef](#)]
35. Li, Y.; Liang, B.; Gu, Z.; Zou, X.; Cheng, J. Unidirectional acoustic transmission through a prism with near-zero refractive index. *Appl. Phys. Lett.* **2013**, *103*, 053505. [[CrossRef](#)]
36. Zhang, T.; Bok, E.; Tomoda, M.; Matsuda, O.; Guo, J.; Liu, X.; Wright, O.B. Compact acoustic metamaterial based on the 3D Mie resonance of a maze ball with an octahedral structure. *Appl. Phys. Lett.* **2022**, *120*, 161701. [[CrossRef](#)]
37. Jia, Y.; Luo, Y.; Wu, D.; Wei, Q.; Liu, X. Enhanced Low-Frequency Monopole and Dipole Acoustic Antennas Based on a Subwavelength Bianisotropic Structure. *Adv. Mater. Technol.* **2020**, *5*, 1900970. [[CrossRef](#)]
38. Dal Poggetto, V.F.; Bosia, F.; Urban, D.; Beoletto, P.H.; Torgersen, J.; Pugno, N.M.; Gliozzi, A.S. Cochlea-inspired tonotopic resonators. *Mater. Des.* **2023**, *227*, 111712. [[CrossRef](#)]
39. Cummer, S.A.; Christensen, J.; Alù, A. Controlling sound with acoustic metamaterials. *Nat. Rev. Mater.* **2016**, *1*, 16001. [[CrossRef](#)]
40. Huang, S.; Lin, Y.; Tang, W.; Deng, R.; He, Q.; Gu, F.; Ball, A.D. Sensing with sound enhanced acoustic metamaterials for fault diagnosis. *Front. Phys.* **2022**, *10*, 1027895. [[CrossRef](#)]
41. Zhu, X.; Liang, B.; Kan, W.; Peng, Y.-G.; Cheng, J. Deep-Subwavelength-Scale Directional Sensing Based on Highly Localized Dipolar Mie Resonances. *Phys. Rev. Appl.* **2016**, *5*, 054015. [[CrossRef](#)]
42. Agulló, J.; Barjau, A.; Keefe, D.H.J.A. Acoustic propagation in flaring, axisymmetric horns: I. A new family of unidimensional solutions. *Acta Acust. United Acust.* **1999**, *85*, 278–284.
43. Orduña-Bustamante, F.; Rendón, P.L.; Martínez-Montejo, E. Comparison between acoustic measurements of brass instruments and one-dimensional models with curved wavefronts and transformed axial coordinates. *J. Acoust. Soc. Am.* **2017**, *142*, 1717. [[CrossRef](#)] [[PubMed](#)]
44. Ma, H.; Shang, T.; Li, G.; Li, Z. Low-frequency sound source localization in enclosed space based on time reversal method. *Measurement* **2022**, *204*, 112096. [[CrossRef](#)]
45. Huang, W.; Wang, D.; Garcia, H.; Godø, O.R.; Ratilal, P. Continental Shelf-Scale Passive Acoustic Detection and Characterization of Diesel-Electric Ships Using a Coherent Hydrophone Array. *Remote Sens.* **2017**, *9*, 772. [[CrossRef](#)]
46. Avots, E.; Vecvanags, A.; Filipovs, J.; Brauns, A.; Skudrins, G.; Done, G.; Ozolins, J.; Anbarjafari, G.; Jakovels, D. Towards Automated Detection and Localization of Red Deer Cervus elaphus Using Passive Acoustic Sensors during the Rut. *Remote Sens.* **2022**, *14*, 2464. [[CrossRef](#)]
47. Buchan, S.J.; Duran, M.; Rojas, C.; Wuth, J.; Mahu, R.; Stafford, K.M.; Becerra Yoma, N. An HMM-DNN-Based System for the Detection and Classification of Low-Frequency Acoustic Signals from Baleen Whales, Earthquakes, and Air Guns off Chile. *Remote Sens.* **2023**, *15*, 2554. [[CrossRef](#)]
48. Shi, Y.; Qiao, Z.; Wang, G.; Wei, J. In Situ Experimental Study of Cloud-Precipitation Interference by Low-Frequency Acoustic Waves. *Remote Sens.* **2023**, *15*, 993. [[CrossRef](#)]
49. Guo, Y.; Zhu, H.; Dang, X. Tracking multiple acoustic sources by adaptive fusion of TDOAs across microphone pairs. *Digit. Signal Process.* **2020**, *106*, 102853. [[CrossRef](#)]

Disclaimer/Publisher's Note: The statements, opinions and data contained in all publications are solely those of the individual author(s) and contributor(s) and not of MDPI and/or the editor(s). MDPI and/or the editor(s) disclaim responsibility for any injury to people or property resulting from any ideas, methods, instructions or products referred to in the content.